Acta Crystallographica Section A
Foundations of Crystallography
ISSN 0108-7673

Charge density and chemical bonding in rutile, TiO_2

B. Jiang,[a]* J. M. Zuo,[b] N. Jiang,[a] M. O'Keeffe[c] and J. C. H. Spence[a]

[a]Department of Physics and Astronomy, Arizona State University, Tempe, AZ 85287-1504, USA, [b]Department of Material Science and Engineering, University of Illinois, Urbana, IL 61801, USA, and [c]Department of Chemistry, Arizona State University, Tempe, AZ 85287, USA. Correspondence e-mail: jiangb@asu.edu

Received 18 February 2003
Accepted 20 May 2003

The low-order structure factors of rutile (TiO_2) have been measured with an accuracy of up to 0.09% by quantitative convergent-beam electron diffraction (QCBED). This error is an order of magnitude smaller than that in conventional Bragg X-ray diffraction and equivalent to the accuracy of the X-ray *Pendellösung* method. It is sufficient to distinguish atomic, covalent and ionic bonding. By refinement of the combined data of low-order reflections measured by electron diffraction with high-order reflections from X-ray diffraction, accurate charge-density maps are obtained and used to understand the role of the 3*d* electrons in Ti—O bonding. The results are combined with electron energy-loss spectra (EELS) in a study of the electronic structure.

1. Introduction

Rutile has a tetragonal ($P4_2/mnm$) structure, one of the simplest structure types, which can be fully described by a (unit-cell constant), c/a and u (internal coordinate). The formal d^0 electron configuration of the Ti atom (in its highest oxidation state) is accompanied by a small lattice distortion responsible for many interesting physical properties. For example, in ferroelectric perovskites such as $BaTiO_3$ and $PbTiO_3$, Ti atoms have the d^0 electron configuration. Cohen (1990) has demonstrated that the hybridization that occurs between the titanium 3*d* states and the oxygen 2*p* states is essential for ferroelectricity in $BaTiO_3$ and $PbTiO_3$ crystals and is the driving force for the TiO_6 oxygen octahedral distortion. His calculations also suggest that Ti^{IV} is not fully ionized as a Ti^{4+} ion. If a spherical-ion model without covalency were assumed, there would be no ferroelectricity. The simple structure of rutile provides an opportunity for studying the Ti—O bond by measurement of the charge distribution in the unit cell. To fully understand the role of valence electrons in the bonding, accurate low-order X-ray structure factors are essential. It is generally believed that an accuracy in measurement of better than 1% is needed in order to see bonding effects. Experimental measurements on rutile have been published by several groups using the Bragg X-ray diffraction method (Shintani *et al.*, 1975; Restori *et al.*, 1987; Gonschorek, 1982; Burdett *et al.*, 1987). However, these measurements are not consistent owing to large extinction effects in the strong low-order reflections. Therefore, it is necessary to use a more accurate method for the low-order reflections in order to obtain a reliable charge-density map and information on the Ti—O chemical bond.

The development of energy-filtered quantitative convergent-beam electron diffraction (QCBED) (Spence & Zuo, 1992; Zuo, 1998) should make accurate low-order structure-factor measurement possible for rutile. The QCBED method fits the experimental intensity profiles within the CBED discs (rocking curves) against multiple scattering calculations (Zuo, 1998). The advantage of electron diffraction is that it is more sensitive at low scattering angles than X-ray diffraction, making it more suitable for the study of bonding (Spence & Zuo, 1992). This technique also takes advantage of a small probe (of nanometre dimensions, smaller than one mosaic block) in a transmission electron microscope (TEM). When combined with the imaging power of TEM, one can find a defect-free crystalline region for electron diffraction experiments, to which the perfect-crystal Bloch-wave theory can be applied. This technique refines structure factors, absorption coefficients and the specimen thickness using full dynamical calculations, and thus measures the structure factors on an absolute scale (Zuo, 1998). Therefore, extinction correction, absorption correction and scaling problems are avoided in the electron diffraction method (Spence & Zuo, 1992; Zuo, 1998; Jiang *et al.*, 2002). Using this technique, Zuo *et al.* (1999) have observed the charge density associated with d_{z^2}-orbital holes and Cu—Cu bonding in crystalline Cu_2O. The high accuracy of QCBED has frequently been used to test the predictions of electronic structure calculation (Zuo, O'Keeffe, Rez & Spence, 1997; Zuo, Blaha & Schwarz, 1997; Saunders *et al.*, 1999; Friis *et al.*, 2003).

In this paper, we present our QCBED measurement of the low-order structure factors of rutile. By combining these measurement with X-ray measurement of high-order reflections, accurate charge deformation maps are obtained. They are used to understand the role of the 3*d* electrons in Ti—O bonding and to explain the crystal structure, electronic structure and incipient ferroelectricity of rutile. These results, as well as electron energy-loss spectra (EELS), are also used to study the electronic structure of rutile. §§2, 3 and 4 explain our experimental method, and the QCBED and multipole refinement techniques. §§5 and 6 show our results for low-order reflection measurement by QCBED multipole refinement and discuss the role of the Ti 3*d* electrons in Ti—O bonding. §7 summarizes our conclusions.

2. Experiment

CBED data were collected on a Leo-912B electron microscope with an in-column Ω filter and a Gatan MSC CCD camera. The high voltage was calibrated to be 119.60 keV (Friis *et al.*, 2003). Diffraction astigmatism is corrected using a standard aluminium sample until no observable astigmatism remained in selected-area diffraction ring patterns. The CCD camera was characterized and the point spread function (PSF) introduced by the CCD into the experimental CBED patterns was properly deconvoluted before refinement (Jiang *et al.*, 2003; Zuo, 1996, 1998). EELS spectra were acquired using a Philips EM400 TEM with field emission gun (FEG) and Gatan 667 parallel electron energy-loss spectrometer (PEELS). The energy resolution is about 0.8 eV.

Rutile crystals are sensitive to radiation damage. The conventional TEM preparation method using ion beam thinning always results in oxygen-deficient layers on the surface. Therefore, crushed samples were used to avoid artifacts from sample preparation. Large thin areas of crystal could then be found easily from the samples. The thickness variation at the thin wedges of crystal can, however, introduce systematic errors. This problem is similar to the earlier finding that CBED patterns from wedge-shaped crystals may not display the correct space group, since the CBED diffraction pattern displays the symmetry of the entire sample, including its boundary conditions, which may destroy crystal symmetry elements (Goodman, 1974).

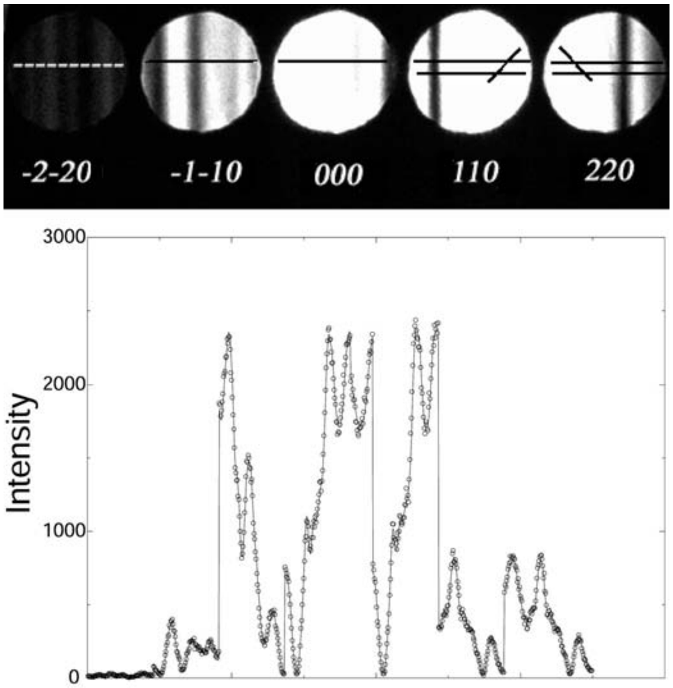

Figure 1
The top image shows the systematic row for 110 and 220 of rutile together with the line scans used. The graph below shows the pixel values (circles) compared with calculated values (solid line). The χ^2 for this fit is 1.2.

To reduce these errors due to thickness changes of the wedge profile under the probe, the line scans in the CBED disc were selected running parallel to the thickness fringes of the sample. This is normally done on thin wedge-shaped samples, with the line of Bragg reflections (systematics) running parallel to the thickness fringes, so that the thickness along the line scan is constant. The CBED data collected in this way will produce better goodness-of-fit (GOF), smaller standard deviation and more reasonable structure factors. Errors will remain if the thickness varies within this line scan. To reduce possible random errors, several CBED patterns were recorded from different regions of the specimen.

Accurate temperature factors (or Debye–Waller factors) are needed for accurate refinement of structure factors (Saunders *et al.*, 1999). The conversion of electron structure factors to X-ray structure factors depends on the temperature factors used (Spence & Zuo, 1992). Incorrect temperature factors will introduce systematic errors in the converted X-ray structure factors and will finally produce an inaccurate charge-density map of the crystal.

In this work, the temperature factors for rutile were obtained from the high-order X-ray diffraction data of Restori *et al.* (1987), measured at 100 K, since the high orders are most sensitive to temperature factors and less affected by extinction (extinction coefficient $y_{\rm ext}$ is close to unity). A multipole refinement software package, *VALRAY* (Stewart *et al.*, 2000), was used for refinement. The neutral atom model of Su & Coppens (1998) was used. A total of 21 independent temperature coefficients, up to the fourth order in the Gram–Charlier expansion (Johnson & Levy, 1974) were refined. The refined temperature factors were quite close to the published values (Restori *et al.*, 1987). The temperature factors at other temperatures (around 100 K) were calculated using the Debye approximation (Coppens, 1997).

Band-theory calculations were performed using full-potential (linearized) augmented plane-wave [(L)APW] + local orbitals (lo) method (L/APW+lo) as embodied in the *WIEN2K* code (Schwarz *et al.*, 2002). Muffin tin radii of 2.0 a.u. for the Ti atom and 1.6 a.u. for the O atoms were used.

3. Low-order structure-factor refinement by QCBED

The program *EXTAL* was used for the refinement (Zuo, 1998). The simplex method was used for minimization searches. The best fit criterion used was the goodness-of-fit quantity χ^2, defined as

$$\chi^2 = \frac{1}{N-f-1}\sum_{i=1}^{N}\frac{I_i^{(\rm exp)} - cI_i^{(\rm theo)} - I^{(\rm bgr)}}{\sigma_i^2},$$

where N is the number of data points, f the number of refined parameters, c a scaling factor, σ the standard deviation of the

Table 1
QCBED measurement on (110) and (220) structure factors of rutile crystal.

U(110) and *U*(220) are the elastic electron structure factors and $Ua_{(110)}$ and $Ua_{(220)}$ are the absorption part. Three data sets measured from (111) zone [(110) systematics] and (001) zone [(110) and $(1\bar{1}0)$ systematics]. [Note: for one-dimensional QCBED, the crystal is tilted to a two-beam condition where only a few beams are excited. If only 110 and 220 reflections are excited, it is called (110) systematics.]

		χ^2	Thickness (Å)	$U_{(110)}$	$Ua_{(110)}$	$U_{(220)}$	$Ua_{(220)}$
Crystal 1	(110)	2.11	1305	0.06349	0.00185	0.04322	0.00161
(111)	systematics	1.28	915	0.06347	0.00169	0.04338	0.00130
zone axis	(tilt 8°)	1.55	908	0.06348	0.00142	0.04350	0.00132
		1.56	982	0.06349	0.00151	0.04338	0.00132
Crystal 2	(110)	1.17	802	0.06354	0.00128	0.04285	0.00127
(001)	systematics	1.05	801	0.06360	0.00125	0.04300	0.00123
zone axis	(tilt 7°)	1.87	970	0.06321	0.00140	0.04334	0.00142
		1.76	1251	0.06331	0.00155	0.04291	0.00131
	$(1\bar{1}0)$	4.29	1076	0.06388	0.00151	0.04304	0.00124
	systematics	2.53	865	0.06341	0.00137	0.04298	0.00114
	(tilt 8°)	2.47	860	0.06334	0.00136	0.04282	0.00123
		3.92	1077	0.06380	0.00132	0.04324	0.00101
Average (12 data)				0.0635 ±0.0002 (±0.3%)	0.00146 ±0.00017	0.0431 ±0.00024 (±0.6%)	0.00133 ±0.00021

experimental intensities and $I_i^{(\mathrm{exp})}$, $I_i^{(\mathrm{theo})}$ and $I^{(\mathrm{bgr})}$ the experimental, theoretical and background intensities, respectively. The sum extends over all pixels in the line scans shown in Fig. 1. The refined parameters are the structure factors (including absorption), beam direction ($\mathbf{k}_t$), scaling factor *c*, background intensity $I^{(\mathrm{bgr})}$ (which is assumed constant for each disc) and sample thickness.

Beams were selected for either diagonalization or perturbation treatment according to three criteria (Zuo & Weickenmeier, 1995; Birkeland *et al.*, 1996): (I) proximity to the Ewald sphere ($2KS_g$, where K is the amplitude of the incident electron wavevector, S_g is the excitation error); (II) length of maximum reciprocal-lattice vector ($g_{\max}$); (III) perturbation strength for selection of weak beams ($|2KS_h/U_h|_{\min}$, where U_h is the electron structure factor). $2KS_g$ is used to select beams for inclusion in the structure matrix to be diagonalized. $|2KS_h/U_h|_{\min}$ selects weak beams for treatment by perturbation, while $g_{\max}$ is used as a cut-off parameter for high-order reflections. We find that good convergence can be obtained for rutile by choosing 3.0 Å^2 (for $2KS_g$), 3.5 Å^{-1} (for $g_{\max}$), 35 (for $|2KS_h/U_h|_{\min}$) for these three parameters.

Specimen thicknesses selected for refinement were normally in the range 600–1500 Å. Within this thickness range, there are enough thickness fringes in the CBED discs to determine the thickness accurately.

The electron-beam direction (k_t) is an important refinement parameter in the *EXTAL* software for accurate structure-factor refinement (Zuo, 1998). Because the lattice parameters are important for determining the HOLZ line positions which are used to refine k_t, accurate lattice constants are needed. Rutile has been studied by several groups using X-ray and neutron diffraction (Burdett *et al.*, 1987; Gonschorek, 1982; Restori *et al.*, 1987). Accurate crystal constants and atomic coordinates at different temperatures are available.

The quality and reproducibility of the QCBED data were tested by comparing three data sets on (110) systematics (see Table 1), recorded from different crystals or from equivalent reflections of the same crystal. The results agree well with each other. These data come from different thicknesses and beam directions (k_t). The small standard deviation clearly indicates the accuracy of the QCBED technique.

4. Multipole refinement

4.1. Combining X-ray diffraction and QCBED data

To combine electron and X-ray diffraction data, first the Bragg X-ray diffraction data of Restori *et al.* (1987) was fitted to correct for extinction, then the low-order reflections were replaced by electron diffraction measurements.

The electron diffraction was collected at a different temperature (107 K) from the X-ray data (100 K) (Restori *et al.*, 1987). Since the temperature increase due to electron illumination is unknown, the real specimen temperature has to be determined. Electron structure factors measured by QCBED have to be converted into X-ray structure factors at the electron diffraction temperature, and then converted to their value at 100 K. According to our measurements on copper, the beam heating for Cu (Friis *et al.*, 2003) due to convergent electron-beam illumination is 5.3 K. It is expected that, for rutile crystals supported by lacy carbon copper grid films, the specimen heating should be higher than that of copper metal. Temperatures from 100 to 130 K were used to convert the electron structure factors to X-ray structure factors. Refinement results of the combined data set showed that the residual and weighted residual were similar for temperatures in the range between 105 and 120 K. Higher or lower temperatures gave a larger residual. The actual specimen temperature was estimated to be 113 K. The temperature increase due to electron illumination is thus about 6 K under our experimental conditions. The error introduced by using incorrect temperature factors could be

Table 2
QCBED refinement results.

The X-ray structure factors were converted from electron structure factors using the Mott–Bethe formula. The theoretical calculations are compared with experimental data. The residual is given by comparison with QCBED experimental data. (Note: the electron diffraction experiment is conducted at 113 K, while the temperature of all the X-ray structure factors is 100 K).

		Measurement by QCBED				Theoretical calculations			
Reflection	d (Å)	χ^2	U_g (Å^{-2}) ±σ% (113 K)	F^x [e (unit cell)$^{-1}$] (100 K)	Best fit (*VALRAY*) (100 K)	Neutral-atom model (100 K)	$\mathrm{Ti}^{2+}\mathrm{O}_2^{1-}$ ionic model (100 K)	$\mathrm{Ti}^{4+}\mathrm{O}_2^{2-}$ ionic model (100 K)	Band theory (100 K)
110	3.245	1.26	0.0635 ±0.3%	37.28±0.033 ±0.09%	37.321	37.620	37.780	35.65	37.530
101	2.485	1.14	0.0356 ±0.9%	23.43±0.09 ±0.38%	23.77	24.289	24.383	22.40	23.529
200	2.294	1.30	0.0184 ±0.8%	13.27±0.05 ±0.4%	13.44	14.393	14.396	12.40	13.362
111	2.185	1.05	0.0267 ±0.2%	18.71±0.04 ±0.2%	18.76	17.985	18.201	18.78	18.822
211	1.686	1.20	0.0360 ±1.4%	30.32±0.2 ±0.66%	30.23	30.278	30.349	30.34	30.214
220	1.622	1.26	0.04314 ±0.6%	34.17±0.15 ±0.44%	34.28	34.519	34.531	34.13	34.640
002	1.478	0.96	0.04785 ±0.33%	38.00±0.12 ±0.3%	38.20	38.090	37.963	37.66	38.055
301	1.359	1.10	0.0401 ±0.6%	32.97±0.22 ±0.67%	33.16	33.239	33.064	33.10	33.279
112	1.345	1.10	0.02484 ±0.4%	23.58±0.06 ±0.25%	23.67	23.749	23.677	23.73	23.759
202	1.243	1.14	0.00628 ±2.3%	12.16±0.2 ±1.6%	12.06	12.077	12.117	12.15	12.113
R (%)					0.48	1.6	1.4	1.6	0.61

estimated. For a 10 K increase (around 100 K), temperature factors will increase by 3%, changes for converted X-ray structure factors using the Mott formula are less than 0.02% for low orders (for 110 and 101 reflections) and 0.35% for high orders (for 301 and 202 reflections), all within experimental errors. Therefore, the uncertainty due to electron beam heating has a small effect under our experimental conditions.

4.2. Multipole refinement and charge-density deformation map

The multipole model (non-spherical pseudoatom model) provides the most efficient parameterization of the real-space charge density (Coppens, 1997). It adopts the classical concept of orbitals in isolated atoms (for monopoles) and high-order multipole parameters that reflect the non-spherical deformation of the valence charge density. The refinement parameters are the monopole populations, the multipole populations and the corresponding radial κ parameters that reflect the contraction or expansion of the radial wavefunctions.

Multipoles up to fourth order and the corresponding radial κ parameters were refined together. Multipoles allowed under the Ti (*mmm*) and O (2*mm*) site symmetries are selected according to the index-picking rules of Kurki-Suonio (1977). All the allowed multipoles were included in the refinement. For the coordinate system shown in Fig. 2, the Ti atoms have five multipoles (*P*20, *P*22+, *P*40, *P*42+, *P*44+) and O atoms have eight multipoles (*P*10, *P*20, *P*22+, *P*30, *P*32+, *P*40, *P*42+, *P*44+). The multipoles on the Ti site were constructed using the $3d$*$3d$ orbitals. On the O site, the dipoles and quadrupoles were constructed from $2s$*$2p$ and $2p$*$2p$ orbitals, and single exponential functions used for the octopoles and hexadecapoles. A total of 17 multipole parameters were refined. Considering only the reflections that are sensitive to the structure factors, there were about 40 beams up to $|g| = 1.1$ Å^{-1} for which the X-ray structure factors change by more than 0.5% when comparing the neutral and ionic models directly. This is enough to determine the 17 multipole parameters.

Different atomic wavefunctions from different calculations were tested to refine the combined data set. The calculation of Su & Coppens (1998) using relativistic calculations gives a better fit than the non-relativistic Hartree–Fock (HF) calculation of Clementi & Roetti (1974).

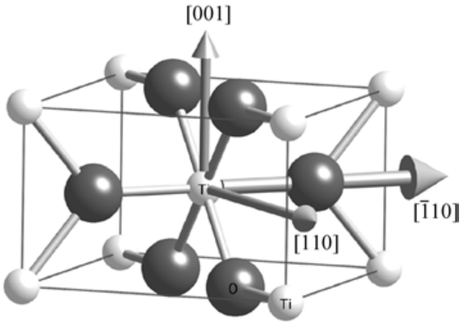

Figure 2
Coordinate system used for multipole refinement and $3d$-orbital population calculations. The coordinate system is defined as: x//[001], y//[110], z//[$\bar{1}$10].

Table 3
Refined multipole parameters obtained from combined data (low-order electron data and high-order X-ray data) and band-theory-calculated structure factors.

Multipole radial functions are constructed from neutral-atom orbital radial functions. (see text for details). Band-theory-calculated structure-factor data are refined using the same model as the combined data set. The smaller residual of the band-theory calculation validates the multipole model on the TiO_2 crystal. Note that the larger κ value for the Ti atom indicates a larger contraction of the Ti valence shell.

	Experiment		Band theory	
Refinement parameters	Ti	O	Ti	O
P_{00}	2.62 (1)	6.69 (2)	2.96 (1)	6.652 (11)
P_{10}	NA	−0.08 (3)	NA	−0.04 (1)
P_{20}	0.29 (7)	0.20 (3)	0.04 (3)	0.03 (1)
P_{22}	0.35 (5)	−0.018 (18)	0.2 (2)	−0.054 (7)
P_{30}	NA	−0.34 (11)	NA	−0.11 (3)
P_{32}	NA	−1.26 (37)	NA	−0.03 (1)
P_{40}	0.25 (7)	−0.77 (35)	0.43 (4)	0.01 (1)
P_{42}	−0.12 (7)	−0.61 (22)	−0.04 (3)	−0.10 (8)
P_{44}	−0.64 (8)	0.35 (31)	−0.66 (1)	−0.16 (10)
$\kappa_0 = \kappa_2 = \kappa_4$	1.13 (2)	NA	1.08 (1)	NA
$\kappa_0 = \kappa_1 = \kappa_2$	NA	0.957 (2)	NA	0.980 (1)
$\alpha_3 = \alpha_4$	NA	3.4 (2)	NA	3.6 (2)
$R(\|F\|)$ (%)	0.89		0.34	

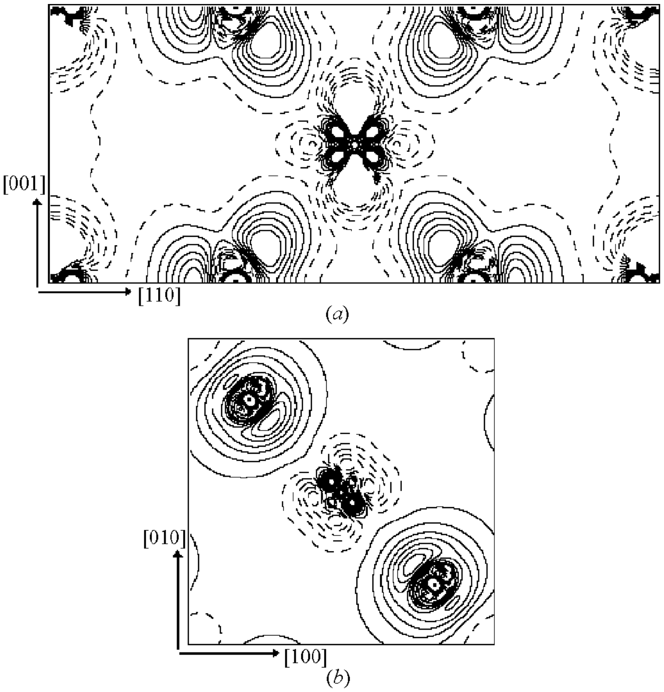

(*a*)

(*b*)

Figure 3
Experimental charge-density difference map of the rutile crystal using combined X-ray and electron data sets (using the neutral-atom model as reference). Dashed contours are for $\Delta\rho < 0$; solid contours are for $\Delta\rho > 0$. The contour values range from −0.4 to 0.4 e Å^{-3} with an increment of 0.05 e Å^{-3}. The cell dimensions are a = b = 4.58895, c = 2.95579 Å (Restori *et al.*, 1987). (*a*) The charge-density deformation map for the (110) plane that passes through the center Ti atom shown in Fig. 2. (*b*) The charge-density deformation map of the (001) plane that passes through the center Ti atom shown in Fig. 2.

The charge-density maps were calculated using the refined multipole parameters in direct space. Charge deformation maps were obtained by subtracting the charge density of the spherical neutral-atom model from our measured density in direct space.

5. Results

5.1. Low-order structure-factor measurement results

The ten strongest low-order reflections that have the largest extinction ($y_{\rm ext} < 0.95$) were measured by the QCBED method (Table 2). The average value and standard deviation of the electron structure factors were obtained by averaging several – normally about six to twelve – experimental measurements. The standard deviation was normally smaller than 0.5% for low orders. The measured standard deviation of the converted X-ray structure factors decreases for low orders owing to the Mott formula (Spence & Zuo, 1992). The standard deviation of the 110 X-ray structure factor is 0.09%, which is equivalent to the accuracy of the X-ray *Pendellösung* method as applied to crystalline silicon (Aldred & Hart, 1973).

X-ray structure factors derived from different theoretical models were compared with our QCBED measurement. For the spherical neutral-atom or ionic model, a large structure-factor change is noticed owing to charge transfer between titanium and oxygen for the first four reflections (see Table 2).

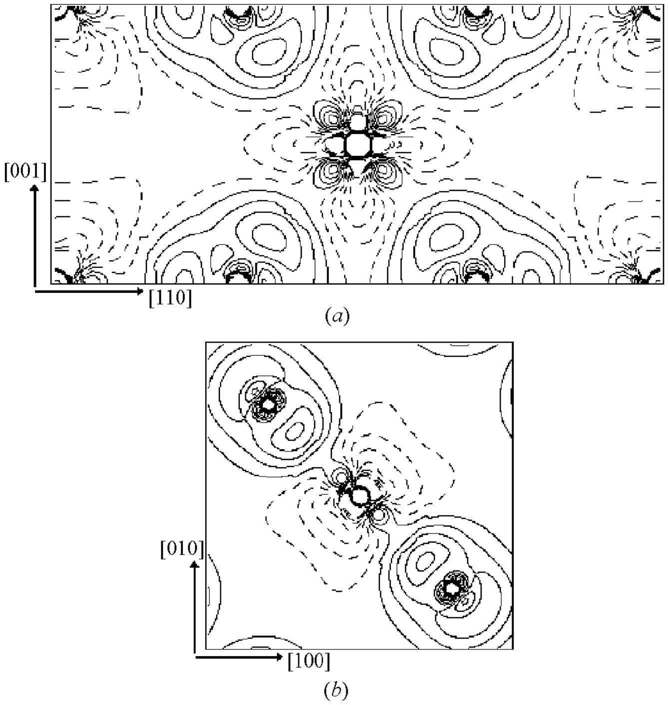

(*a*)

(*b*)

Figure 4
Charge-density difference map calculated using FLAPW (GGA96 approach) (Schwarz *et al.*, 2002). Dashed contours are for $\Delta\rho < 0$; solid contours are for $\Delta\rho > 0$. The contour values range from −0.4 to 0.4 e Å^{-3} with an increment of 0.05 e Å^{-3} (using the neutral-atom model as reference). (*a*) The charge-density deformation map of the (110) plane. (*b*) The charge-density deformation map of the (001) plane.

Table 4
The calculated Ti-atom 3*d* orbital populations from multipole parameters in Table 3.

The coordinate system is defined in Fig. 2. Note: we assume zero occupancy for 4*s* and 4*p* orbitals.

Orbital	
d_{z^2}	0.645 (35)
d_{xy}	0.669 (37)
d_{xz}	0.501 (46)
d_{yz}	0.479 (46)
$d_{x^2-y^2}$	0.328 (37)
$d_{z^2}d_{x^2-y^2}$	−0.149 (44)
Total electron population	2.62 (1)

None of these spherical models gives a reasonable fit to the measured structure factors. However, a good fit between the QCBED experimental results and a band-structure calculation is found [*WIEN2K* code (Schwarz *et al.*, 2002)].

5.2. Multipole refinement results

The multipole refinement results are listed in Table 3. The overall fit is improved for the combined electron and X-ray data, compared with that using X-ray diffraction data alone. It is seen that the improvement of the fit for the low-order reflections as measured by QCBED is significant (see Table 2). The residual of ten electron diffraction reflections becomes smaller (0.48%) (see Table 2), it is also smaller than the residual of the full data set (which is 0.89%) (see Table 3), indicating improvement of the electron diffraction measurement over X-ray diffraction. Compared with the X-ray dataset refinement, the internal consistency is improved; the difference between the measured data and the fitted data becomes smaller for these ten low-order reflections measured by QCBED. A large improvement is observed particularly for the 110, 002, 200, 211, 301 reflections, for which extinction effects are very strong ($y_{\rm ext} < 0.95$). This more accurate combined data set can be used for an accurate charge-density study. The structure-factor data set calculated by band theory (L/APW+lo method) (Schwarz *et al.*, 2002) was also fitted using the same model as the combined data set (see Table 3), and it was observed that the Ti-atom monopole population became larger than the experimental measurement. The smaller residual of 0.34% for the band-theory calculation validates the multipole model for the TiO$_2$ crystal.

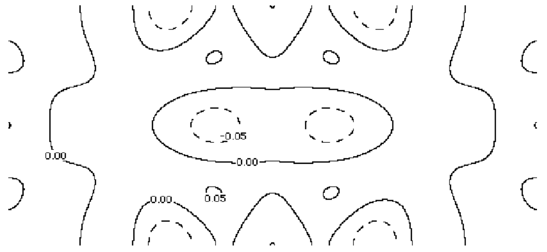

Figure 5
Residual map of the (110) plane. Only low-order reflections measured by QCBED are used. The contour level is 0.05 e Å^{-3}. Dashed contours are for $\Delta\rho < 0$; the solid contours are for $\Delta\rho > 0$. The largest variation is ±0.05 e Å^{-3}.

Charge-density deformation maps obtained using *VALRAY* are plotted in Fig. 3. They show several features of the Ti–O bonding. (I) Charge deficiency at the Ti-atom site and charge surplus at the O-atom site indicate charge transfer between Ti and O atoms (ionic bonding). (II) The stronger charge-deficiency region at the Ti-atom site along the crystal *c* direction resembles a d_{x^2}-type orbital hole (Fig. 3*a*). (III) A non-spherical valence-shell charge distribution representing covalent bonding is seen on both O and Ti atoms. It is seen that feature (II) is not observed in charge deformation maps by band-theory calculation (see Fig. 4).

The population of the individual Ti 3*d* orbitals can be calculated from the multipole populations (Holladay *et al.*, 1983). The 3*d*-orbital population depends on the coordinate system used. The results are listed in Table 4.

Error analysis can help determine which features in the experimental charge-density map are reliable. Residual and variance maps were calculated to study the errors. A variance map gives the noise level, which for most of the area is 0.08 e Å^{-3}, except for the nuclear region (within 0.5 Å radius). The residual map looks featureless (Fig. 5).

6. Discussion

6.1. Accuracy of experimental QCBED

For crystals, only valence electrons contribute to bonding, and these affect reflections at low scattering angles ($s = \sin\theta/\lambda < 0.5$). Changes of X-ray structure factors due to bonding are small, normally less than 1% for low-order reflections. Thus, high experimental accuracy for low-order reflections is needed to see bonding features. The accuracy needed in low-order reflections should be sufficient to identify

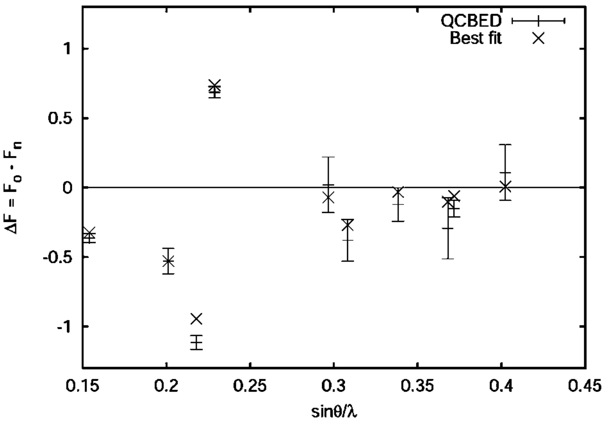

Figure 6
Difference of X-ray structure factors between the QCBED measurement and the neutral-atom model *versus* scattering angle ($s = \sin\theta/\lambda$). The *Y* axis represents the difference of X-ray structure factors between QCBED measurement and the neutral-atom model (in units of electrons per unit cell). Note the consistency between QCBED best fit values from multipole refinement. (Only reflections measured by QCBED are shown.)

the difference between a crystal and a neutral-atom model. Thus the measurement error must be smaller than the difference between the structure factors of these two models in order to see bonding features.

Accuracy in the QCBED method was tested for the 110 and 220 reflections (see Table 1). It was thereby proved to be a robust method. Errors are the estimated standard deviation for many measurements from different specimen areas and different crystal tilts with different thickness. Fig. 6 shows the X-ray structure-factor differences between the measured and a neutral-atom model, as well as the experimental errors. It is seen that only low-order reflections with small scattering angles ($s < 0.3$) have changed more than 0.1 electron per unit cell. Experimental errors in these low-order reflections are much smaller than the differences between the experimental values and those for a neutral-atom model. The data set is thus accurate enough to identify bonding features in rutile. Consistency of the experimental and the best fit from multipole refinement is also observed (Fig. 6).

6.2. Molecular-orbital diagram and electronic structure of TiO_2

In rutile TiO_2, Ti atoms are surrounded by six O atoms, forming a distorted octahedron. Therefore, Ti 3*d* orbitals will split into two sets of e_g and t_{2g} orbitals. We use the notation (e_g, t_{2g}) appropriate for $m\bar{3}m$ symmetry, even though the real symmetry at Ti is reduced to *mmm*. The O atoms are surrounded by three Ti atoms in a planar geometry, thus sp^2 hybridization of the O atom forms three σ bonds (from p_x, p_y and *s* orbitals) in the plane and one π bond (from p_z) perpendicular to the plane (for the coordinate system shown in Fig. 2). According to the molecular-orbital (MO) diagram of the TiO_6 octahedral complex (shown in Fig. 7) (Sorantin & Schwartz, 1992), two Ti e_g orbitals combining with Ti sp^3 orbitals will form six σ metal–ligand bonds pointing to the six O atoms, and form molecular orbitals. (Note that we use the coordinate system shown in Fig. 2, *x* and *y* directions are not along the Ti—O bond, d_{z^2} and d_{xy} orbitals belong to e_g orbitals, d_{xz}, d_{yz} and $d_{x^2-y^2}$ orbitals belong to t_{2g} orbitals.) The d_{yz} orbitals form a π bond with the apical oxygen p_z orbital, while the d_{xz} and $d_{x^2-y^2}$ orbitals have σ non-bonding with O atoms or form π or σ bonds with the Ti atom in the *x* direction depending on the metal-atom distance. This Ti—Ti bonding is expected to be very weak owing to the large distance between Ti metal atoms.

This molecular-orbital approach has been very successful for the qualitative interpretation of the O *K*-edge EELS and XPS spectra of TiO_2 (Grunes *et al.*, 1971). Fig. 8 shows an EELS spectrum of the O *K* edge in rutile TiO_2. There are two relatively sharp peaks at 537.0 and 539.7 eV. These two are due to the unoccupied orbitals of Ti t_{2g} hybridized with O $2p\pi$, and Ti e_g with O $2sp^2\sigma$, respectively. At higher energies (between 543 and 556 eV), there is a broad maximum with three recognizable features marked as **a** (546.3 eV), **b** (548.9 eV) and **c** (551.4 eV), respectively. These features are assigned to the hybridized orbitals of O *p* with Ti *s* and *p* states.

The bonding character of TiO_2 has also been studied based on band-structure calculations (Schwarz *et al.*, 2002). For comparison, the calculated EELS of the O *K* edge is also plotted in Fig. 8. The spectra have been aligned to the position of the first peak. It is seen that the major features are reproduced by the calculations, although the core hole effect is not included in the calculation. [Calculations that include a core hole (Z+1 approximation) show little difference in the O *K* edge from those without core hole.]

Fig. 9 gives the projected density of states (DOS) for TiO_2. In general, the band-structure calculations are in agreement with the molecular-orbital analysis. However, de Groot *et al.* (1989) pointed out that the peak between 543 and 556 eV (Fig.

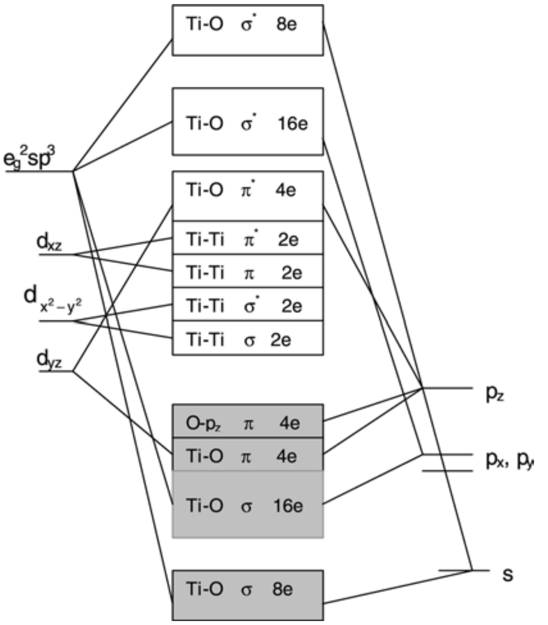

Figure 7
Molecular-orbital scheme for rutile (Ti_2O_4). The energy levels occupied in rutile are represented by gray shadings. The coordinate systems used for the atoms are shown in Fig. 2.

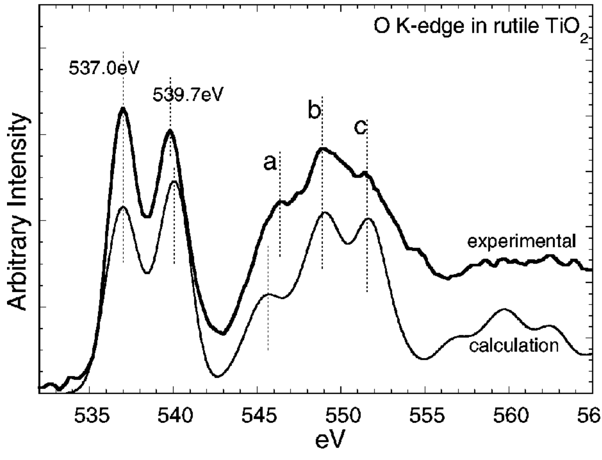

Figure 8
Comparison of experimental EELS of O *K* edge with theoretical calculations using the *WIEN2K* code. The two spectra are aligned to the first peak at 537.0 eV.

8) is dominated by oxygen p character and can be assigned to direct oxygen–oxygen interactions. More precisely, we assign peaks **b** and **c** in Fig. 8 to the interactions of O p states with Ti s, p and d bands. This is because the Ti s, p and d bands have high intensities at the positions of peaks **b** and **c**, as shown in Fig. 9. Peak **a**, on the other hand, cannot be simply assigned to any Ti band; it is dominated by the O p states. However, we found no evidence of O—O bonding in the charge-density map (Fig. 3).

6.3. Ti 3*d* orbital population, chemical bonding and charge deformation maps in rutile

For Ti, with site symmetry *mmm* in rutile, a 6 × 6 matrix was used to convert the multipole populations to the five canonical d-orbital population of d_{z^2}, d_{xy}, d_{yz}, d_{xz} and $d_{x^2-y^2}$, plus a mixed term, $d_{z^2}d_{x^2-y^2}$ (O'Toole & Streltsov, 2001). These orbital populations (Table 4) were obtained by the method of Coppens (1997). The total Ti valence population (monopole) is 2.62. To obtain individual d-orbital occupancy, we assume zero occupancy for 4s and 4p orbitals. The mixed term should be zero if the point group has 4/*mmm* symmetry and non-zero in the symmetrical case of *mmm* symmetry (O'Toole & Streltsov, 2001). According to our local coordinate system (Fig. 2), the z direction is along the long Ti—O bond direction. This is the closest local coordinate system to 4/*mmm* point-group symmetry. The calculated mixed term is close to zero (Table 4). Thus the Ti site symmetry is very close to 4/*mmm* symmetry for this local coordinate system. Similar results can be found for the rutile structures of ZnF_2 and CoF_2 crystals (O'Toole & Streltsov, 2001).

The 3d-orbital populations for the Ti atom show the role of the 3d electrons in Ti—O bonding. For e_g orbitals, the d_{xy} orbital has somewhat more electron population than the d_{z^2} orbital, forming the strongest bond with oxygen (short Ti—O σ bond in Fig. 3*a*), pointing to the four equatorial oxygen atoms; the d_{z^2} orbital forms the second strongest bond with the apical oxygen atom (long Ti—O σ bond in Fig. 3*b*). For the other three t_{2g} orbitals, the d_{xz} orbital has weak bonding with the apical oxygen; the d_{yz} has some electron concentration compared with neutral atoms, which suggests that there is weak π bonding between Ti atoms in the y direction (the bond distance is 2.95 Å); the $d_{x^2-y^2}$ orbitals have fewer electrons than a neutral atom, suggesting the absence of σ bonding between Ti atoms in the y direction.

Fig. 10 shows the density of states (DOS) of rutile with the following features: (I) the bands between −6 and 0 eV are mainly from oxygen 2p orbitals; (II) the bands above Fermi energy are dominated by contributions from Ti 3d orbitals; (III) band hybridization occurs mainly at the bottom of the valence band for Ti 3d and O 2p valence electrons, at the top of the valence band we find mostly non-overlapping O 2p electrons. These characters agree with current experimental findings: charge transfer from Ti to O atoms from features (I)

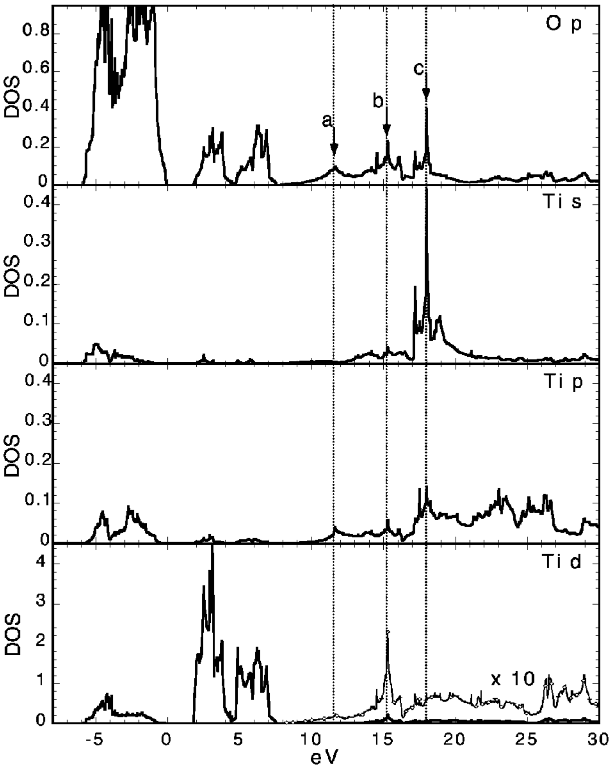

Figure 9
The projected density of states of rutile TiO_2. The vertical lines are guides.

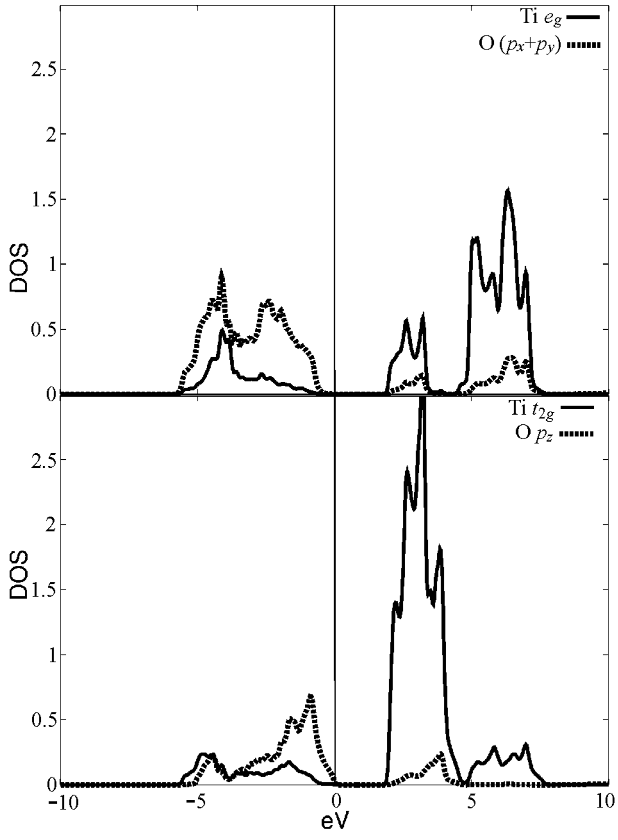

Figure 10
Decomposition of TiO_2 density of states (DOS) into symmetry-projected Ti e_g + O p_x + p_y, and Ti t_{2g} + O p_z contributions. The Fermi level is at 0 eV (vertical line).

and (II), only O 2p electrons at the bottom of the valence band contributing to the Ti—O σ bond from feature (III).

The Ti—O bond can be seen in the charge-density deformation map. We note from Fig. 3 that both ionic and covalent bonding play a role in Ti—O bonding. The ionic and covalent bonding stem from the charge transfer between Ti and O atoms and the hybridization of Ti 3d and oxygen 2p orbitals, respectively. The main features of the charge deformation map from experiment and band theory are quite similar. The electron charge peaks between the Ti—O short and long bonds are 0.41 and 0.30 e Å^{-3}, respectively (Figs. 3a, b). These values are higher than the band-structure calculation, which is 0.22 and 0.21 e Å^{-3}, respectively (Figs. 4a, b). The variance analysis gives a 0.08 e Å^{-3} e.s.d. (low boundary of the e.s.d.) in the experimental charge-density map and the residual map showed a ±0.05 e Å^{-3} variation (Fig. 5). By considering these measurement errors, we find that the measured and theoretical charge deformation maps are in close agreement. The position of the charge peaks in the experimental maps are closer to the oxygen nuclei than in the band calculated maps. Multipole refinement also shows that the Ti monopole is larger for the band-theory calculation (see Table 3), indicating less charge transfer from the Ti atom to the O atom for the theory calculation than in the experimental measurement. These results suggest that Ti—O bonding is more ionic than predicted by band theory.

6.4. Crystal structure, soft mode and incipient ferroelectricity

We note in Table 2 that the low orders are very sensitive to the charge transfer between Ti and O atoms, but none of the spherical neutral-atom or ionic models could fit the QCBED data. This indicates the importance of the multipole contribution, which shows a large contribution from Ti—O covalent bonding. The band-theory calculation suggests that Ti e_g hybridize with O p_x+p_y orbitals to form covalent bonds, while t_{2g} hybridize with O p_z to form weak π bonds. Thus the rutile structure results from the combined effect of covalency and electrostatics. A simple model proposed by O'Keeffe (1977) predicts rutile crystal parameters very well by considering both covalency (fixing the cation–anion distance) and the electrostatic anion–anion repulsion (maximizing the unit-cell volume). The use of solely an electrostatic (ionic) or a covalent (MO) model cannot explain the lattice deformation.

The ferroelectric soft mode in TiO_2 is the $A_{2u}(\Gamma_1)$ mode. In this mode, the Ti atom [at $(\frac{1}{2},\frac{1}{2},\frac{1}{2})$] moves along the [001] direction. The corresponding bond affected is the short Ti—O σ bond (the d_{xy}-orbital electron is responsible for this bonding). With decreasing temperature from 300 to 4 K, the soft-mode frequency decreases from 172 to 142 cm^{-1} and, with increasing pressure, the soft mode becomes hardened (Samara & Peercy, 1973). The static dielectric constant is very high along the crystal [001] direction. All these properties conform with the properties observed in ferroelectric crystals (such as $BaTiO_3$).

Ferroelectricity is considered to be a second-order Jahn–Teller effect, in which oxygen octahedral distortion favors a stable low-symmetry polar phase. Weyrich (1990) and Weyrich & Madenach (1990) have demonstrated that Ti and O valence-electron hybridization occurs mainly at the bottom of the valence band for cubic phase crystalline $BaTiO_3$; the top of the valence band is mostly O 2p non-hybridized electrons. O-atom octahedral distortion and Ti-atom shift increase the hybridization on the top of the valence band for O 2p and Ti 3d orbitals, with electron transfer from O to Ti atoms (compared with the cubic phase). The increasing hybridization of O 2p and Ti 3d orbitals lowers the $BaTiO_3$ total energy. Rutile has a similar electronic structure to cubic $BaTiO_3$ for the Ti 3d and O 2p orbitals (from Fig. 10). The incipient ferroelectricity for rutile TiO_2 may indicate the tendency for increasing Ti 3d and O 2p orbital hybridization.

It is interesting that the size of the oxygen octahedra (determined by Ti—O bond length) is critical for the ferroelectric phase to occur, as can be seen by comparison with the cubic phases of $SrTiO_3$ and $BaTiO_3$. For $SrTiO_3$ and $BaTiO_3$, the Ti—O bond lengths are 1.955 and 2.008 Å, respectively. FLAPW calculations on $BaTiO_3$ show that a shorter Ti—O distance (less than 1.985 Å) would stabilize the cubic phase (Cohen, 1990). Ti—O bonds in rutile have an average distance of 1.959 Å (four short bonds and two long bonds, oxygen octahedra in rutile are distorted), close to those in $SrTiO_3$. This implies that the Ti—O distance may play an important role in ferroelectricity in these crystals.

The QCBED method for charge-density refinement and multipole analysis might thus be used to help understand paraelectricity and ferroelectricity in these materials by mapping the charge density along the Ti—O bond. If combined with other experimental techniques for electronic structure analysis such as X-ray emission spectroscopy and EELS (or X-ray absorption spectroscopy), these would form a powerful approach to the study of ferroelectricity.

7. Conclusions

Low-order structure factors of rutile have been measured by the QCBED method, giving an order of magnitude improvement in accuracy for low-order reflections. Charge deformation maps were then refined by using *VALRAY* software, combing electron and X-ray diffraction data. Several features were found in the charge deformation maps, a d_{x^2}-type orbital hole on the Ti atoms, and ionic and covalent bonding in the Ti—O bond. The Ti—O covalent bond is discussed in the MO scheme. Good agreement was obtained with FLAPW calculations, with an R factor of 0.61%. The agreement changes little with different exchange–correlation potential models. These accurate charge-density maps can be used to help understand the rutile geometry and incipient ferroelectricity.

This research was funded by DOE DE-FG03-02ER45596. JMZ is supported by DOE DEFG02-01ER45923 and DEFG02-91ER45439. We thank Professors R. F. Stewart of

Carnegie Mellon University, Pittsburgh, PA, USA, and University of Copenhagen, Denmark, and Claude Lecomte (Nancy, France) for helpful discussions. We thank Professor Schwarzenbach (Université de Lausanne, Switzerland) for kindly supplying the X-ray structure factors (reference: Restori *et al.*, 1987). Thanks to Claus Flensburg for help on the *VALRAY* software. The experiments were done at the Center for High Resolution Electron Microscopy (CHREM) of Arizona State University.

References

Aldred, P. J. & Hart, M. (1973). *Proc. R. Soc. London Ser. A*, **332**, 223–238.

Birkeland, R., Holmestad, K. M. & Høier, R. (1996). *Ultramicroscopy*, **66**, 89–99.

Burdett, J. K., Hughbanks, T., Miller, G. J., Richardson, J. W. & Smith, J. V. (1987). *J. Am. Chem. Soc.* **109**, 3639–3646.

Clementi, E. & Roetti, C. (1974). *At. Data Nucl. Data Tables*, **14**, 177–478.

Cohen, R. E. (1990). *Nature (London)*, **258**, 136–138.

Coppens, P. (1997). *X-ray Charge Density and Chemical Bonding.* Oxford University Press.

Friis, J., Jiang, B., Spence, J. C. H. & Holmestad, R. (2003). *Microsc. Microanal.* In the press.

Gonschorek, W. (1982). *Z. Kristallogr.* **160**, 187–203.

Goodman, P. (1974). *Nature (London)*, **251**, 698–701.

Groot, F. M. F. de, Grioni, M., Fuggle, J. C., Sawatzky, G. A. & Petersen, H. (1989). *Phys. Rev. B*, **40**, 5715–5723.

Grunes, L. A., Leapman, R. D., Wilker, C. N., Hoffman, R. & Kunz, A. B. (1971). *Phys. Rev. B*, **25**, 7517.

Holladay, A., Leung, P. & Coppens, P. (1983). *Acta Cryst.* A**39**, 377–387.

Jiang, B., Zuo, J. M., Chen, Q. & Spence, J. C. H. (2002). *Acta Cryst.* A**58**, 4–11.

Jiang, B., Zuo, J. M., Friis, J. & Spence, J. C. H. (2003). *Microsc. Microanal.* In the press.

Johnson, C. K. & Levy, H. A. (1974). *International Tables for X-ray Crystallography*, Vol. IV, pp. 312–336. Birmingham, England: Kynoch Press.

Kurki-Suonio, K. (1977). *Isr. J. Chem.* **16**, 115–123.

O'Keeffe, M. (1977). *Acta Cryst.* A**33**, 924–927.

O'Toole, N. J. & Streltsov, A. (2001). *Acta Cryst.* B**57**, 128–135.

Restori, R., Schwarzenbach, D. & Schneider, J. R. (1987). *Acta Cryst.* B**43**, 251–257.

Samara, G. & Peercy, P. S. (1973). *Phys. Rev. B*, **7**(3), 1131–1148.

Saunders, M., Fox, A. G. & Midgley, P. A. (1999). *Acta Cryst.* A**55**, 471–479.

Schwarz, K., Blaha, P. & Madsen, G. K. H. (2002). *Comput. Phys. Commun.* **147**, 71–76.

Shintani, H., Sato, S. & Saito, Y. (1975). *Acta Cryst.* B**31**, 1981–1982.

Sorantin, P. & Schwartz, K. (1992). *Inorg. Chem.* **31**, 567–576.

Spence, J. C. H. & Zuo, J. M. (1992). *Electron Microdiffraction.* New York: Plenum Press.

Stewart, R. F., Spackman, M. A. & Flensburg, C. (2000). *VALRAY User's Manual.* Carnegie Mellon University, Pittsburgh, PA, USA, and University of Copenhagen, Denmark.

Su, Z. W. & Coppens, P. (1998). *Acta Cryst.* A**54**, 646–652.

Weyrich, K. H. (1990). *Ferroelectrics*, **104**, 183–194.

Weyrich, K. H. & Madenach, P. (1990). *Ferroelectrics*, **111**, 9–14.

Zuo, J. M. (1996). *Ultramicroscopy*, **66**, 21–33.

Zuo, J. M. (1998). *Mater. Trans. Jpn Inst. Met.* **39**, 938–946.

Zuo, J. M., Blaha, P. & Schwarz, K. (1997). *J. Phys. Condens. Matter*, **9**, 7541–7561.

Zuo, J. M., Kim, M., O'Keeffe, M. & Spence, J. C. H. (1999). *Nature (London)*, **401**, 49–52.

Zuo, J. M., O'Keeffe, M., Rez, P. & Spence, J. C. H. (1997). *Phys. Rev. Lett.* **78**, 4777–4780.

Zuo, J. M. & Weickenmeier, A. (1995). *Ultramicroscopy*, **57**, 375–383.